POLITECNICO DI TORINO
Repository ISTITUZIONALE

Composite polymer electrolyte with high inorganic additive contents to enable metallic lithium anode

Original
Composite polymer electrolyte with high inorganic additive contents to enable metallic lithium anode / Amici, J.; Calderon, C. A.; Versaci, D.; Luque, G.; Barraco, D.; Leiva, E.; Francia, C.; Bodoardo, S.. - In: ELECTROCHIMICA ACTA. - ISSN 0013-4686. - ELETTRONICO. - 404:(2022), p. 139772. [10.1016/j.electacta.2021.139772]

Availability:
This version is available at: 11583/2971396 since: 2022-09-18T15:33:21Z

Publisher:
Elsevier Ltd

Published
DOI:10.1016/j.electacta.2021.139772

Terms of use:

This article is made available under terms and conditions as specified in the corresponding bibliographic description in the repository

Publisher copyright
Elsevier postprint/Author's Accepted Manuscript

© 2022. This manuscript version is made available under the CC-BY-NC-ND 4.0 license http://creativecommons.org/licenses/by-nc-nd/4.0/.The final authenticated version is available online at: http://dx.doi.org/10.1016/j.electacta.2021.139772

(Article begins on next page)

18 September 2024

Composite polymer electrolyte with high inorganic additive contents to enable metallic lithium anode

Julia Amici[1*], Cecilia Andrea Calderón[2*], Daniele Versaci[1], Guillermina Luque[3], Daniel Barraco[2], Ezequiel Leiva[3], Carlotta Francia[1], Silvia Bodoardo[1]

[1] *Politecnico di Torino, Department of Applied Science and Technology, Electrochemistry Group, Corso Duca degli Abruzzi, 24, 10129 Turín, Italia.*

[2]*Instituto de Física Enrique Gaviola, Facultad de Matemática, Astronomía, Física y Computación, Universidad Nacional de Córdoba, Av. Medina Allende s/n, ciudad universitaria, Córdoba, Argentina.*

[3]*Instituto de Investigaciones en Fisicoquímica de Córdoba, Facultad de Ciencias Químicas, Universidad Nacional de Córdoba, Haya de la Torre esq. Medina Allende, Ciudad Universitaria, Córdoba, Argentina.*

**Both authors contributed equally to this work*

Abstract

Composite polymer electrolytes (CPE) are a very promising strategy for using lithium metal anodes safely. These electrolytes are formed by polymeric matrices in which ceramic nanoparticles are incorporated to modify their mechanical and conduction properties. In this work a methacrylate-based polymer matrix containing 63 wt% of ZrO_2 nanoparticles (NPs) was prepared and tested as electrolyte for lithium metal batteries. The prepared CPE shows a higher ionic conductivity than the polymer matrix without ZrO_2 NPs and a higher lithium transport number than Celgard with liquid electrolyte and stabilizes the processes of deposition-dissolution of lithium with respect to the reference cell, thus prolonging the cycling time without short circuits. Finally, the compatibility of the CPE with a $LiFePO_4$ cathode was verified, achieving a stable cycling at 1.0 C and at ambient temperature, with an impressive capacity of 140.18 mAh g^{-1} even after 250 cycles.

Keywords: *Composite polymer electrolytes, metallic lithium, polymer crosslinking, thermal activation, inorganic additive.*

Acronyms

BMA: butyl methacrylate
BPO: benzoyl peroxide
CPE: composite polymer electrolyte
DEC: diethyl carbonate
EC: Ethylene carbonate
NMP: N-methyl pyrrolidone
PEGDA: polyethylene glycol diacrylate

PVDF: polyvinylidene fluoride
SEI: solid-electrolyte interphase

1 Introduction

Li-ion batteries specific energy density is now nearly approaching its theoretical values, after growing by about 7 Wh kg^{-1} per year in the last 25 years [1]**.** A rechargeable battery-specific energy density is primarily determined by electrodes specific capacity and operating voltage [2,3]. In this perspective, lithium metal anode represents the "holy grail" of battery research for its extremely high theoretical specific capacity (3860 mA h g^{-1}), its lowest redox potential (-3.04 V vs. the standard hydrogen electrode), and low gravimetric density (0.534 g cm^{-3}). On the other hand, metallic Li being thermodynamically unstable in all liquid electrolytes immediately forms a solid-electrolyte interphase (SEI) when immersed into electrolyte [4]. Peled was the first to describe this phenomenon of an ionically conductive and electrically insulating interface in 1979 [5]. As the reduction potential of most organic solvents is below 1.00 V *vs.* (Li/Li^+), immediate reactions between Li and electrolyte take place in a time of milliseconds when bare Li is exposed to an electrolytic solution [4]. An ideal SEI should inhibit the further reaction between Li and electrolytes and suppress the Li dendrite formation. However, spontaneously formed SEI is fragile and heterogeneous with variable spatial resistance, which induces uneven Li-ions flow and random Li deposition underneath [6]. A well-known kinetic model proposes that the presence of Li-ions near Li-metal anode is due to the charge at high current density and drain of Li-salt anions. The ionic concentration approaches zero, from the positive electrode to the negative one, at a time called "Sand's time" [7]. Consequently, lack of Li^+ layer paired with local space charge layer is considered the main reason for dendritic Li growth [8]. Indeed, when ionic concentrations at the anode surface become zero, at Sand's time, cations and anions in the liquid electrolyte show different behaviors, leading to excessive Li^+ ions at the surface [9,10]. At this point, lithium nucleates and grows dendritically as a function of current density and interfacial elastic strength [8]. In the subsequent stripping process, thin Li dendrites may break from the roots forming the so-called "dead Li" [1,11]. Moreover, due to the intrinsic inhomogeneous nature of Li metal and its uncontrolled deposition behavior, Li-ion prefers to deposit on the hot spots because of fast reaction kinetic and shorter diffusion length [12,13].

Therefore, in order to improve the stability of Li metal to be eventually incorporated into practical application, efforts must be made to: (1) suppress the dendrite formation and growth, (2) accommodate and constrain the volume change, and (3) stabilize and optimize the

surface SEI layer [14]. Decades of research on this topic drew the conclusion that the ideal SEI layer should possess high ionic conductivity, relatively small thickness, high Young's modulus and homogeneous surface morphology for deposited lithium [8]. Monroe and Newman conducted different studies on the subject, and they stated that Li dendrites could be effectively suppressed when the interface Young's modulus was about twice higher than the one of the Li anode [15]. Meanwhile, a polymer layer coating on Li foil or separator can serve as artificial SEI with higher shear modulus compared to SEI spontaneously formed in contact with liquid electrolyte. It can alleviate and guide the dendrite formation and improve the Coulombic efficiency, however, it cannot change the features of dendrite growth [16].

A solution to this problem is the use of a solid electrolyte with a very high Young's modulus to efficiently block dendrite formation [14]. Solid ceramic electrolytes are stable and have high Li^+ conductivity but the interface with the electrode is a problem as it is difficult to achieve good contact between electrolyte and electrode [17]. Solid polymeric electrolytes are an alternative that is being widely investigated since their softness compared to ceramic improves the contact with the electrode surface [18]. Moreover, by adjusting the degree of cross-linking of the polymers, the protective layers can further facilitate smooth plating/stripping of Li on the surface of anodes and enable solely Li^+ transport [14]. Polymer electrolytes allow to use several additives to improve their properties, for example, ionic liquids are usually added to the polymer network to improve conductivity [19]. Inorganic fillers are added to different polymer-based electrolyte forming composite polymer electrolytes to improve mechanical strength and ionic conductivity where particle size, physical nature of the filler and filler ratio, play a significant role in the properties of the electrolyte [1]. For instance, a PEO (poly(ethylene oxide)) based CPE containing Al_2O_3 and LiTFSI was prepared and good results were obtained on lithium plating/stripping [20]. The effect of montmorillonite clay mineral additives on the stability and electrochemical performance of LiTFSI in a PVDF-HFP/PMMA/PNIPAM polymer matrix was also investigated observing very good results [21]. Using $LiGe_2(PO_4)_3$ as an additive in polymer membranes based on a dimethacrylic-oligomer (BEMA) resulted in a highly stable lithium plating/stripping reversibility and significantly restrained Li dendrite growth [22].

In this work we present the preparation of a methacrylate-based polymer matrix, in a solvent-free, thermally induced radical polymerization, encompassing ZrO_2 nanoparticles and activated with liquid electrolyte. This method allowed to obtain self-standing and flexible membranes with content up to 80 wt% of additive, demonstrating the feasibility of the "polymer in ceramic" approach. The use of high contents of the inorganic additive permit to enhance mechanical properties avoiding lithium dendrites nucleation and stabilizing Li stripping/platting, hence greatly improving Li metal cell safety. In particular, the optimized

additive content of 63 wt% allows outstanding cycling performances at 1C and room temperature.

2 Experimental

2.1 Preparation of BMA10PEGDA-based membranes

The synthesis is performed in a controlled Ar atmosphere glovebox (O_2 and H_2O contents <0.5 ppm) to avoid oxygen inhibition to radical reaction. The precursor solutions contain the monomer butyl methacrylate (BMA, 99% Acros Organics), the crosslinking agent polyethylene glycol diacrylate (PEGDA575, Mn 575, Aldrich) in a proportion 10% wt., the thermo-initiator benzoyl peroxide (BPO, 75% Acros Organics) and eventually high-purity monoclinic ZrO_2 nanoparticles (NPs) (TZ0 Tosoh Co., Tokyo, Japan) as an additive in different proportions. The mix is heated to 80°C for 30 minutes and cast on a glass slide, then the temperature is kept constant at 45°C for 20 hours and finally increased to 100°C for 2 hours.

2.2 Characterization of BMA10PEGDA-based membranes

Thermal-stability and ZrO_2 final content is assessed by TGA analysis, carried out between 25 °C and 800 °C at a rate of 10 °C·min^{-1} in air (TGA/SDTA-851 instrument, METTLER, Switzerland). Effective cross-linking is indagated through Fourier transform infrared spectroscopy (FTIR) experiments, on a NicoletTM iS50 FTIR spectrometer (Thermo Scientific TM) equipped with an attenuated total reflection (ATR) tool over the range 4000-400 cm^{-1} with a resolution of 4 cm^{-1} at room temperature. The morphologies of the NPs and membranes are observed by the field-emission scanning electron microscopy FE-SEM, ZEISS Supra 40.

The liquid electrolyte uptake (*LEU*) was obtained by measuring the weight of the dry membrane and the saturated membrane after immersion for 2 h in the electrolyte. The electrolyte uptake was calculated according to Eq. (1).

$LEU = ([M_e - M_0]/M_0) \times 100$ (1)

where M_0 and M_e are the weights of the membrane before and after immersion, respectively.

2.3 Cathode preparation

To obtain the $LiFePO_4$ (LFP) electrode as cathode for the cell testing, a slurry is prepared composed of LFP, conductive carbon (C65), and binder (PVDF) mixed in N-methyl pyrrolidone (NMP) with a weight ratio of 7:2:1. Then the slurry is coated on Al foil and dried overnight at room temperature. The as-obtained electrode is cut into 18 mm diameter discs and dried under vacuum, at 120 °C for 4h.

2.4 Electrochemical characterization

To determine ionic conductivity of the membranes, electrochemical impedance spectroscopy (EIS) measurements are performed between 100 kHz and 1 Hz at open-circuit-potential using a CHI potentiostat instrument, Cambria. Cells are assembled in EL-Cell (ECC-Std) with membrane discs of 2.545 cm^2 sandwiched between two stainless steel blocking electrodes of the same area, and the cells are tested between 25 and 70 °C. The ionic conductivity is calculated at each temperature using Eq. (2).

$\sigma = (l/A) * (1/R_{\Omega})$ (2)

where l is the membrane thickness, A is the membrane surface area and R_{Ω} is the resistance of the electrolyte measured at the high-frequency intercept on EIS spectra.

A Li/Li symmetrical cell configuration, with the corresponding membrane (swollen with liquid electrolyte: EC:DEC (1:1) $LiPF_6$) sandwiched in between (ECC-Std), is used to study the effect of the membrane on the lithium plating/stripping phenomenon. A control-cell is assembled as follow Li/Celgard2500 + Liquid Electrolyte/Li (ECC-Std). The initial impedance of the fresh cells is measured in the frequency range from 100 kHz to 1 Hz at open circuit potential, followed by 10 cycles at a current density of 0.1 mA cm^{-2} and related discharge capacity of 0.1 mA·h^{-1} cm^2, followed by EIS measurement, 10 cycles at a current density of 0.5 mA cm^{-2} and related discharge capacity of 0.5 mA·h^{-1} cm^2, followed by EIS measurement and 10 cycles at a current density of 1.0 mA cm^{-2} and related discharge capacity of 1.0 mA·h^{-1} cm^2, followed by EIS measurement, using a CHI potentiostat instrument, Cambria. Afterward, both cells are resumed at a current density of 1.0 mA cm^{-2} and related discharge capacity of 1.0 mA·$h^{-1}cm^2$ for 60 cycles.

The electrochemical stability is evaluated by linear sweep voltammetry (LSV) performed with a SS/Membrane/Li cell (ECC-Std) at a scan rate of 0.5 mV·s^{-1} from 0.0 to 5.5 V *vs*. Li/Li^+ at room-temperature. The lithium-ion transference number (t_{Li+}) is measured by a potentiostatic polarization method using a symmetrical Li–Li cell (Li/Membrane/Li). The lithium-ion transference number t_{Li+} can be calculated by Bruce & Vincent model following Eq. (3) [23]:

$t_{Li+} = [\, I_s \times (\Delta V - I_0 R_0)]/[\, I_0 \times (\Delta V - I_s R_s)]$ (3)

Where I_0 and I_S are the initial and steady-state current, respectively. ΔV is the DC potential (10 mV) applied to chronoamperometry; R_0 and R_S are the interfacial impedance at initial and steady-state, respectively, which are measured with EIS.

For full-cell testing, LFP|Membrane|Li cells are assembled in ECC-Std test cells (EL-CELL GmbH, Germany). Galvanostatic cycling is performed to assess lifetime and rate performances on an Arbin BT-2000 battery tester. All the tests are carried out at room temperature.

3 Results and Discussion

3.1 Membrane characterization

Four different membranes are tested: BMA10PEGDA without additive and three samples with different amounts of ZrO_2 NPs added during polymerization reaction. To determine NPs amount on each membrane as well the thermal stability, TGA measurements were performed. Figure 1 shows TGA curves for the four membranes and for precursors BMA, PEGDA575 and ZrO_2 NPs for comparison. BMA is completely evaporated around 100°C, PEGDA575 is thermally stable until 400°C and ZrO_2 NPs do not show any changes through all temperature intervals. Membranes are thermally stable until 250°C and completely discomposed at 480°C. For membranes with additives, the percentage of added ZrO_2 NPs are 38, 63, and 80 wt% for the samples called BMA10PEGDA38, BMA10PEGDA63, and BMA10PEGDA80 respectively.

Pictures of the membranes are reported on Figure 2. The BMA10PEGDA membrane is thin, transparent, and flexible enough to be folded without breaking (Fig. 2a). The membranes keep their flexibility even after ZrO_2 NPs addition. The membranes are white (Fig. 2b, c and d) showing a homogeneous distribution of the NPs. All the membranes were reticulated onto a glass-slide, then peeled off and were perfectly self-standing.

FTIR spectra for the precursors (ZrO_2 NPs, BMA and PEGDA) and for the membranes are shown on Figure S1. ZrO_2 NPS show no peaks while BMA and PEGDA show the characteristic peak for C=C bond at 1636 cm^{-1} [24]. For all the membranes with and without NPs, the 1636 cm^{-1} peak fades away or disappears which verifies the complete polymerization of monomer and crosslinker in all the samples [25]. XRD spectra show that BMA10PEGDA has some crystallinity which is lost with ZrO_2 addition (Figure S2). The diffraction patterns of the three membranes with NPs show the ZrO_2 diffraction pattern without modifications, so NPs crystallinity is not affected during the membrane preparation (Figure S2).

FESEM micrographs made for BMA10PEGDA and BMA10PEGDA80 for surface and cross-section are reported in Figure 3. BMA10PEGDA shows a smooth and regular morphology on the surface (Figure 3 a and b) with a globular structure on the cross-section image and a

thickness of around 10 μm (Figure 3 c). For BMA10PEGDA80 the surface image shows spherics ZrO_2 NPs agglomeration with a thin layer of polymer covering them (Figure 3 d and e). A solid mix of NPs with polymer is observed on the cross-section image and membrane thickness is around 60 μm (Figure 3 f). ZrO_2 monoclinic NPs were observed with FESEM, the image shows regular spherical shapes with a diameter around 50 nm (Figure S3). *LEU* was assessed for the different samples and is reported in Table S1. The value is much higher in the polymer matrix without additives compared to the other samples, this can be explained by the fact that such values represent a weight percentage on the total membrane weight (including eventual ZrO2 content) while the inorganic portion is not able to absorb any liquid electrolyte.

3.2 Electrochemical characterization

Ionic conductivity of the membranes was determined by EIS measurements in a temperature range from room temperature to 70°C. Ionic conductivity dependence with temperature in Arrhenius expression for the membranes are shown on Figure 4. For all the cases ionic conductivity increases when temperature increases, showing a linear dependence for all ranges studied excepted room temperature. The ionic conductivity notoriously increases by three orders of magnitude when ZrO_2 NPs are added to the membrane. This improved conductivity was expected since ZrO_2 is well known for its high dielectric constant [26]. Therefore, such increase of ionic conductivity can be attributed to an increase in 'free' ions concentration, thanks to a higher degree of salt dissociation, and of re-dissociation of ion aggregates [27]. Similar results were demonstrated by addition of plasticizers with various dielectric constants in a polymer matrix [28] or comparing the effect of varying dielectric constant on the ionic conductivity of PEMA/PVdF-HFP blend films [29].

In particular, comparing BMA10PEGDA38 with BMA10PEGDA63, ionic conductivity increases with ZrO_2 content around one order of magnitude but decreases for BMA10PEGDA80. This behavior, already reported in literature with other kind of additives [30,31], can be explained using the percolation theory (see the Supporting Information for more details). In particular, we demonstrated that an optimum ZrO_2 NPs concentration exists that allows the formation of a continuous percolation chain constituting an ideal pathway for Li ions at the interface between the polymer and the additive (Figure S7) improving the conductivity of the membrane. Higher concentration would then create a physical obstacle for ionic conduction. Because BMA10PEGDA63 shows the highest ionic conductivity, further experiments were performed with this membrane and commercial Celgard2500 impregnated with liquid electrolyte (EC:DEC 1:1 1M $LiPF_6$), as a reference.

The decomposition of the electrolyte at upper voltage is a serious issue affecting both the performance and the safety of Li-metal batteries. Hence, an electrolyte with stable electrochemical window has great significance for the stable operation of such system. The electrochemical windows of BMA10PEGDA63 was assessed by LSV and compared to the one of the reference cell; the results are reported in Figure S4. The results obtained are fairly similar with a stability window up to 4.5 V.

Transport numbers were determined by equation 3 using Bruce & Vincent method [23] for Celgard2500 and BMA10PEGDA63 swollen in the liquid electrolyte (with 148 wt% liquid electrolyte uptake). The transference number t_{Li+} plays an essential role in alleviating the concentration polarization, an important cause of overpotential in batteries [32]. A high t_{Li+} can mitigate the anion accumulation around the interface between electrode and electrolyte, in particular at high current density, thus allowing the electrode polarization to be restrained and lowering the corresponding polarization resistance [33]. The t_{Li+} value of the BMA10PEGDA63 was assessed by a combination of potential polarization and EIS at room temperature (Figure 5b) and compared to the reference (Figure 5a). The results show a value of 0.50 for BMA10PEGDA63 against 0.45 for the reference cell. Such an improvement explains the results obtained for the ionic conductivities, further demonstrating the synergy between the polymer matrix and the ZrO_2 nanoparticles for fast Li^+ ions transfer through the composite electrolyte. Therefore, BMA10PEGDA63 should allow a drastic decrease of concentration gradients, which have been demonstrated in the literature to be one of the principal causes of Li dendrite nucleation and growth [34].

Metal lithium stripping and deposition were investigated for symmetric Li/Li cells. Figure 6 shows the galvanostatic curves for cycling at several current densities and EIS spectra that were taken every 10 cycles. The reference cell with Celgard2500 shows a peaking shape as a result of different kinetic pathways for reactions at the electrode/electrolyte interphase [13]. For an increase in current density, the potential profile shows inconspicuous shape changes but an increase in overpotential as a result of Ohm´s law. For each current density value, the overpotential decreases with cycle number, which could be attributed to an increase of the effective surface area, due to the dissolution-deposition process accumulated on the electrode surface [35]. The potential profile for the cell assembled with BMAPEGDA63 (Figure 6c) shows no peaking shape, even more, the curves for the first 10 cycles show an “increasing arc” profile and after the first 10 cycles the profile is basically flat. This demonstrate a much easier plating/stripping process and stabilized interface [13] The overpotential keeps almost constant when current density increases, which indicates restrained Li dendrite growth and highly stable lithium plating/stripping reversibility [19,22].

EIS spectra show a semicircle which, according to SEI model, is due to the surface film resistance (R_{sf}), where the migration of Li^+ in the surface film is the rate-determining step of Li deposition/dissolution reactions [36]. This is confirmed because the characteristic frequency for each spectrum (Table S2) is much lower than that for the charge-transfer process of the Li/Li^+ redox couple (several kHz) [36].

EIS spectra for the reference cell (Figure 6b) show a big increase on the R_{sf} (low frequency process) after the electrode is cycled 10 times at 0.1 mA cm^{-2} with respect to the initial cell. This first increase on R_{sf} is due to the accumulation of new SEI and dead lithium at the interphase [36]. This SEI layer inhibits the chemical reactions that continue to occur on the surface of the active Li electrode and thus helps to improve related properties of the cell [31]. However, R_{sf} decreases after the electrode is cycled 10 times at 0.5 and 1.0 mA cm^{-2}. The decrease on R_{sf} at higher currents is due to the increase of surface area, and confirmed by the decrease of overpotential on galvanostatic curves [35].

EIS spectra for the cell assembled with BMA10PEGDA63 show an increase in R_{sf} (low frequency process) after cycling the cell 10 times at 0.1mA cm^{-2}, and a decrease in R_{sf} after cycling at 0.5 and 1.0 mA cm^{-2} (Figure 6d), just like the reference cell. However, the decrease in R_{sf} is less pronounced for the cell with BMA10PEGDA63 with respect to the reference. This indicates that, although there is an increase in the electroactive surface area due to the accumulation of structures during stripping-deposition cycles, this increase is attenuated for the cell with BMA10PEGDA63, confirming the effectiveness of the membrane in reducing the formation of high surface area lithium (HSAL).

Figure 6e shows long cycling at 1.0 mA cm^{-2}, the control cell presents short circuits after 46 hours of cycling, while the cell assembled with BMA10PEGDA63 was cycled for 60 hours without short-circuiting. This result demonstrates that the membrane effectively allows increasing the cell cyclability.

The cycling performance of the BMA10PEGDA63 in a complete cell was tested with LFP cathodes at room temperature. Figure 7a shows the potential profile for a LFP-Li cell with Celgard and with BMA10PEGDA63. The overpotential for the cell assembled with the membrane is significantly smaller than for Celgard2500. As was previously discussed, the transport number for BMA10PEGDA63 (0.50) is higher than for Celgard2500 (0.45), due to its role in alleviating the anion accumulation. The higher t_{Li+} is thus responsible for the lower overpotential during battery cycling [32]. As a direct consequence, after 250 cycles at 1C, the capacity of the first one is still 140.18 mAh g^{-1} while the capacity of the second one is only 121.61 mAh g^{-1} (Figure 7 b). To further assess this difference, the voltage profile for the two cells for different cycle numbers at 1 C is reported in Figure S5, and the voltage hysteresis is

calculated at the fixed capacity of 60 mAh g^{-1} and reported in Table S3. The value of the overvoltage between charge and discharge is much lower, from the first cycle on, in the BMA10PEGDA63 cell, and remains smaller than half of the overvoltage of the Celgard2500 cell, up to the 250th cycle. Moreover, observing the values of the Celgard2500 cell, we can note that the overvoltage initially decreases between the 1st and the 25th cycles but successively increases constantly from the 25th to the 250th cycle. This phenomenon further confirms the previous results: in the Celgard2500 cell no stable interface is formed between the electrolyte and the Lithium anode, dendrites are formed and successively broken thus forming dead Li and progressively increasing the resistance of the interface and therefore the cell polarization. On the contrary, in the BMA10PEGDA63 cell the overvoltage remains low and quite constant over 250 cycles demonstrating a reduced polarization and confirming the influence of the higher t_{Li+} number with an improved Li^+ transfer kinetics [37]. Figure S6 shows capacity evolution for a long-term cycling at 0.1 C; for this lower rate both cells deliver almost the same capacity. The differences in the first cycles could be attributable to a phenomenon of cell formation in the one containing the Celgard2500 separator. After 70 cycles the BMA10PEGDA63 cell retains a capacity of 145.89 mAh g^{-1}, while the Celgard2500 cell retains a capacity of 144.67 mAh g^{-1}, thus not representing a noticeable difference. As was previously discussed, a high t_{Li+} can mitigate the anion accumulation on the interface particularly for high current density; therefore, its effect is evident for higher current density and not obvious at lower ones.

The cells rate capability was also tested; and results are shown in Figure 8. The BMA10PEGDA63 cell (Figure 8b) holds outstanding rate capacities of 167, 163, 154, and 148 mAh/g at different rates from 0.1 C to 1C with a recovery of 162 mAh/g back at 0.1C corresponding to 97% of capacity recovery, thus validating its good reversibility and cyclability. Meanwhile, comparing discharge and charge capacities, we can see that the coulombic efficiency remains almost 100%, illustrating that the composite electrolyte can afford high current density operation because of its excellent ability to limit Li dendrites growth and form a stable SEI film, in line with the previously detailed results. Consequently, the cell polarization trend can be restrained, thus lowering the corresponding polarization, enabling higher capacity retention at higher current density [33]. In comparison, the standard cell (with Celgard2500) demonstrated lower rate capacities of 161, 153, 144, and 132 mAh/g at the corresponding C-rates with a recovery of 155 mAh/g at 1C, corresponding to 96% of capacity recovery (Figure 8a).

4 Conclusions

In conclusion, thanks to thermo-initiated, solvent-free, free radical polymerization, we were able to obtain cross-linked composite polymer electrolyte containing up to 80 wt % of ZrO_2 NPs with optimal mechanical properties. The membrane containing the optimized content of 63 wt% of additive showed the best electrochemical properties with a high ionic conductivity and a high t_{Li+} number, confirming its ability to limit ionic concentration gradients in the electrolyte. This resulted in a much smoother Lithium plating and deposition process, as compared with a reference cell containing commercial Celgard and liquid electrolyte. Such optimal electrochemical properties, allowed to obtain stable cycling, at 1.0 C and at ambient temperature with a capacity as high as 140.18 mAh g^{-1} even after 250 cycles for LFP cathodes, thus demonstrating the efficiency of the "ceramic in polymer" approach as composite electrolyte for Li-metal batteries.

Acknowledgements

The authors wish to thank Mauro Raimondo from Politecnico of Torino for the FESEM, and the POLAR project (progetto per l'internazionalizzazione della ricerca tra Politecnico di Torino e Argentina, prof Silvia Bodoardo) for the funding.

References

[1] X.-Q. Zhang, X.-B. Cheng, Q. Zhang, Advances in Interfaces between Li Metal Anode and Electrolyte, Adv. Mater. Interfaces. 5 (2018) 1701097. https://doi.org/10.1002/admi.201701097.

[2] G. Ganas, G. Kastrinaki, D. Zarvalis, G. Karagiannakis, A.G. Konstandopoulos, D. Versaci, S. Bodoardo, Synthesis and characterization of LNMO cathode materials for lithium-ion batteries, Mater. Today Proc. 5 (2018) 27416–27424. https://doi.org/10.1016/j.matpr.2018.09.059.

[3] D. Versaci, A. Costanzo, S.M. Ronchetti, B. Onida, J. Amici, C. Francia, S. Bodoardo, Ultrasmall SnO2 directly grown on commercial C45 carbon as lithium-ion battery anodes for long cycling performance, Electrochim. Acta. 367 (2021) 137489. https://doi.org/10.1016/j.electacta.2020.137489.

[4] H. Yang, C. Guo, A. Naveed, J. Lei, J. Yang, Y. Nuli, J. Wang, Recent progress and perspective on lithium metal anode protection, Energy Storage Mater. 14 (2018) 199–221. https://doi.org/10.1016/j.ensm.2018.03.001.

[5] E. Peled, The Electrochemical Behavior of Alkali and Alkaline Earth Metals in Nonaqueous Battery Systems—The Solid Electrolyte Interphase Model, J. Electrochem. Soc. 126 (1979) 2047–2051. https://doi.org/10.1149/1.2128859.

[6] K. Chen, D.-Y. Yang, G. Huang, X.-B. Zhang, Lithium–Air Batteries: Air-Electrochemistry and Anode Stabilization, Acc. Chem. Res. 54 (2021) 632–641. https://doi.org/10.1021/acs.accounts.0c00772.

[7] J.-N. Chazalviel, Electrochemical aspects of the generation of ramified metallic

electrodeposits, Phys. Rev. A. 42 (1990) 7355–7367. https://doi.org/10.1103/PhysRevA.42.7355.

[8] K. Zhang, G.-H. Lee, M. Park, W. Li, Y.-M. Kang, Recent Developments of the Lithium Metal Anode for Rechargeable Non-Aqueous Batteries, Adv. Energy Mater. 6 (2016) 1600811. https://doi.org/10.1002/aenm.201600811.

[9] M. Rosso, C. Brissot, A. Teyssot, M. Dollé, L. Sannier, J.-M. Tarascon, R. Bouchet, S. Lascaud, Dendrite short-circuit and fuse effect on Li/polymer/Li cells, Electrochim. Acta. 51 (2006) 5334–5340. https://doi.org/10.1016/j.electacta.2006.02.004.

[10] C. Brissot, M. Rosso, J. -N. Chazalviel, S. Lascaud, In Situ Concentration Cartography in the Neighborhood of Dendrites Growing in Lithium/Polymer-Electrolyte/Lithium Cells, J. Electrochem. Soc. 146 (1999) 4393–4400. https://doi.org/10.1149/1.1392649.

[11] K. Chen, K.N. Wood, E. Kazyak, W.S. Lepage, A.L. Davis, J. Sanchez, N.P. Dasgupta, Dead lithium: mass transport effects on voltage, capacity, and failure of lithium metal anodes, J. Mater. Chem. A Mater. Energy Sustain. 5 (2017) 11671–11681. https://doi.org/10.1039/c7ta00371d.

[12] K.N. Wood, M. Noked, N.P. Dasgupta, Lithium Metal Anodes: Toward an Improved Understanding of Coupled Morphological, Electrochemical, and Mechanical Behavior, ACS Energy Lett. 2 (2017) 664–672. https://doi.org/10.1021/acsenergylett.6b00650.

[13] K.N. Wood, E. Kazyak, A.F. Chadwick, K.H. Chen, J.G. Zhang, K. Thornton, N.P. Dasgupta, Dendrites and pits: Untangling the complex behavior of lithium metal anodes through operando video microscopy, ACS Cent. Sci. 2 (2016) 790–801. https://doi.org/10.1021/acscentsci.6b00260.

[14] Y. Wang, E. Sahadeo, G. Rubloff, C.-F. Lin, S.B. Lee, High-capacity lithium sulfur battery and beyond: a review of metal anode protection layers and perspective of solid-state electrolytes, J. Mater. Sci. 54 (2019) 3671–3693. https://doi.org/10.1007/s10853-018-3093-7.

[15] C. Monroe, J. Newman, The Impact of Elastic Deformation on Deposition Kinetics at Lithium/Polymer Interfaces, J. Electrochem. Soc. 152 (2005) A396. https://doi.org/10.1149/1.1850854.

[16] X.Q. Zhang, X.B. Cheng, Q. Zhang, Advances in Interfaces between Li Metal Anode and Electrolyte, Adv. Mater. Interfaces. 5 (2018) 1–19. https://doi.org/10.1002/admi.201701097.

[17] C.Z. Zhao, B.C. Zhao, C. Yan, X.Q. Zhang, J.Q. Huang, Y. Mo, X. Xu, H. Li, Q. Zhang, Liquid phase therapy to solid electrolyte–electrode interface in solid-state Li metal batteries: A review, Energy Storage Mater. 24 (2020) 75–84. https://doi.org/10.1016/j.ensm.2019.07.026.

[18] Q. Zhang, K. Liu, F. Ding, X. Liu, Recent advances in solid polymer electrolytes for lithium, Nano Res. 1 (2017) 1–36.

[19] C.A. Calderón, A. Vizintin, J. Bobnar, D.E. Barraco, E.P.M. Leiva, A. Visintin, S. Fantini, F. Fischer, R. Dominko, Lithium Metal Protection by a Cross-Linked Polymer Ionic Liquid and Its Application in Lithium Battery, ACS Appl. Energy Mater. 3 (2020) 2020–2027. https://doi.org/10.1021/acsaem.9b02309.

[20] X. Judez, G.G. Eshetu, I. Gracia, P. López-Aranguren, J.A. González-Marcos, M. Armand, L.M. Rodriguez-Martinez, H. Zhang, C. Li, Understanding the Role of Nano-Aluminum Oxide in All-Solid-State Lithium-Sulfur Batteries, ChemElectroChem. 6 (2019) 326–330. https://doi.org/10.1002/celc.201801390.

[21] D.E. Fenton, J.M. Parker, P.V. Wright, Complexes of alkali metal ions with poly(ethylene oxide), Polymer (Guildf). 14 (1973) 589. https://doi.org/10.1016/0032-3861(73)90146-8.

[22] J. Amici, S. Romanin, M. Alidoost, D. Versaci, C. Francia, F. Smeacetto, S. Bodoardo, UV-cured methacrylate based polymer composite electrolyte for metallic lithium batteries, J. Electroanal. Chem. 837 (2019) 103–107. https://doi.org/10.1016/j.jelechem.2019.02.027.

[23] S. Andrews, Electrochemical measurement of transference numbers in polymer electrolytes, Polymer (Guildf). 28 (1987) 2324–2328.

[24] J. Zhang, C. Ma, J. Liu, L. Chen, A. Pan, W. Wei, Solid polymer electrolyte membranes based on organic/inorganic nanocomposites with star-shaped structure for high performance lithium ion battery, J. Memb. Sci. 509 (2016) 138–148. https://doi.org/10.1016/j.memsci.2016.02.049.

[25] H. Duan, Y. Yin, X. Zeng, J. Li, J. Shi, Y. Shi, R. Wen, In-situ plasticized polymer electrolyte with double-network for fl exible, Energy Storage Mater. 10 (2018) 85–91. https://doi.org/10.1016/j.ensm.2017.06.017.

[26] P.K. Alaboina, S. Rodrigues, M. Rottmayer, S.-J. Cho, In Situ Dendrite Suppression Study of Nanolayer Encapsulated Li Metal Enabled by Zirconia Atomic Layer Deposition, ACS Appl. Mater. Interfaces. 10 (2018) 32801–32808. https://doi.org/10.1021/acsami.8b08585.

[27] J.M.C. Puguan, W.-J. Chung, H. Kim, Ion-conductive and transparent PVdF-HFP/silane-functionalized ZrO2 nanocomposite electrolyte for electrochromic applications, Electrochim. Acta. 196 (2016) 236–244. https://doi.org/10.1016/j.electacta.2016.02.172.

[28] N.S. Mohamed, A.K. Arof, Investigation of electrical and electrochemical properties of PVDF-based polymer electrolytes, J. Power Sources. 132 (2004) 229–234. https://doi.org/https://doi.org/10.1016/j.jpowsour.2003.12.031.

[29] L.N. Sim, S.R. Majid, A.K. Arof, Characteristics of PEMA/PVdF-HFP blend polymeric gel films incorporated with lithium triflate salt in electrochromic device, Solid State Ionics. 209–210 (2012) 15–23. https://doi.org/10.1016/j.ssi.2011.11.035.

[30] K.M. Kim, N.G. Park, K.S. Ryu, S.H. Chang, Characteristics of PVdF-HFP/TiO2 composite membrane electrolytes prepared by phase inversion and conventional casting methods, Electrochim. Acta. 51 (2006) 5636–5644. https://doi.org/10.1016/j.electacta.2006.02.038.

[31] Q. Guo, Y. Han, H. Wang, S. Xiong, Y. Li, S. Liu, K. Xie, New Class of LAGP-Based Solid Polymer Composite Electrolyte for Efficient and Safe Solid-State Lithium Batteries, ACS Appl. Mater. Interfaces. 9 (2017) 41837–41844. https://doi.org/10.1021/acsami.7b12092.

[32] Z. Qiu, L. Shi, Z. Wang, J. Mindemark, J. Zhu, K. Edström, Y. Zhao, S. Yuan, Surface

activated polyethylene separator promoting Li+ ion transport in gel polymer electrolytes and cycling stability of Li-metal anode, Chem. Eng. J. 368 (2019) 321–330. https://doi.org/10.1016/j.cej.2019.02.107.

[33] S. Wang, L. Zhou, M.K. Tufail, L. Yang, P. Zhai, R. Chen, W. Yang, In-Situ synthesized Non-flammable gel polymer electrolyte enable highly safe and Dendrite-Free lithium metal batteries, Chem. Eng. J. 415 (2021) 128846. https://doi.org/10.1016/j.cej.2021.128846.

[34] K. Xu, Nonaqueous Liquid Electrolytes for Lithium-Based Rechargeable Batteries, Chem. Rev. 104 (2004) 4303–4418. https://doi.org/10.1021/cr030203g.

[35] S. Drvarič Talian, J. Bobnar, A.R. Sinigoj, I. Humar, M. Gaberšček, Transmission Line Model for Description of the Impedance Response of Li Electrodes with Dendritic Growth, J. Phys. Chem. C. 123 (2019) 27997–28007. https://doi.org/10.1021/acs.jpcc.9b05887.

[36] S. Shiraishi, K. Kanamura, Z. Takehara, Surface Condition Changes in Lithium Metal Deposited in Nonaqueous Electrolyte Containing HF by Dissolution-Deposition Cycles, J. Electrochem. Soc. 146 (1999) 1633–1639. https://doi.org/10.1149/1.1391818.

[37] Y. Liang, Y. Liu, D. Chen, L. Dong, Z. Guang, J. Liu, B. Yuan, M. Yang, Y. Dong, Q. Li, C. Yang, D. Tang, W. He, Hydroxyapatite functionalization of solid polymer electrolytes for high-conductivity solid-state lithium-ion batteries, Mater. Today Energy. 20 (2021) 100694. https://doi.org/10.1016/j.mtener.2021.100694.

Figures Captions

Figure 1: TGA measurements for precursors BMA (pink line), PEGDA (blue line), ZrO_2 NPs (yellow line) and for the membranes BMA10PEGDA (black line), BMA10PEGDA38 (green line), BMA10PEGDA63 (red line) BMA10PEGDA80 (violet line).

Figure 2: Pictures of the membranes self-standing and being bent: a) BMA10PEGDA, b) BMA10PEGDA38, c) BMA10PEGDA63, d) BMA10PEGDA80.

Figure 3: FESEM micrographs for BMA10PEGDA (a, b, c), BMA10PEGDA80 (d, e, f) and ZrO_2 NPs (i); c and f are cross section images of the membranes.

Figure 4: Conductivity vs. temperature plot of BMA10PEGDA (red markers), BMA10PEGDA38 (green markers), BMA10PEGDA63 (purple markers) and BMA10PEGDA80 (blue markers). Celgard2500 was added as reference (black markers). Data obtained by impedance measurements.

Figure 5: Current-Time profile of Li/Celgard2500/Li (a) and Li/BMA10PEGDA63/Li (b). The insets show the AC impedance spectra before and after polarization.

Figure 6: Lithium symmetric cells electrochemical experiments for reference cell assembled with Celgard2500 and liquid electrolyte (a and b) and BMAPEGDA63 galvanostatic stripping and deposition at several current density and EIS spectra. e) Long galvanostatic cycling at 1 mA cm^{-2}.

Figure 7: Voltage profile of LFP-Li cells with Celgard2500 (black) and BMA10PEGDA63 (blue) at 1 C (50th cycle), at room temperature (a), Discharge capacities of LFP-Li cells with Celgard2500 and BMA10PEGDA63 at 1 C, at room temperature (b).

Figure 8: Capacity retention of LFP-Li cells with Celgard2500 (a) and BMA10PEGDA63 (b) at different C-rates at room temperature.

Figures

Figure 1

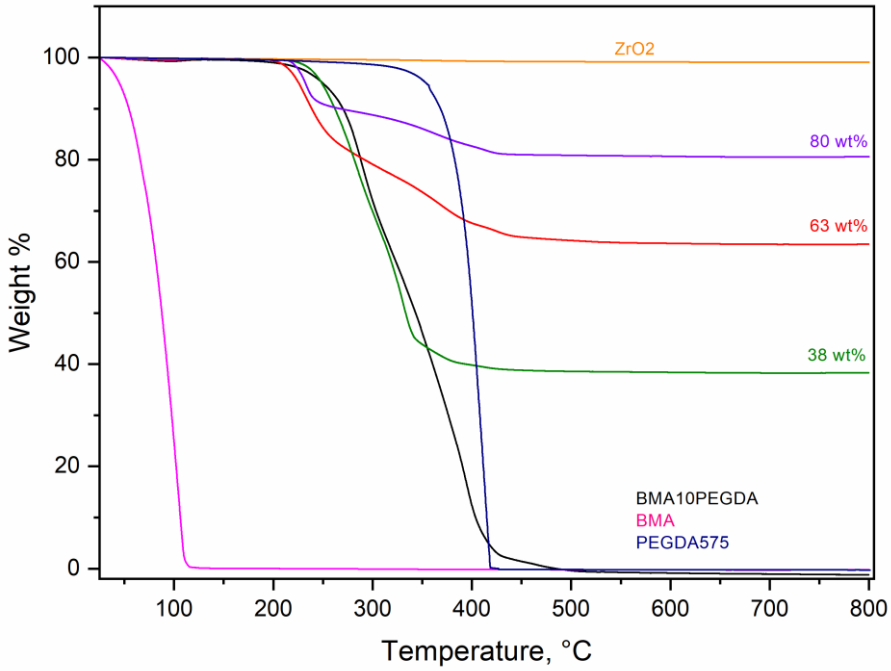

Figure 2

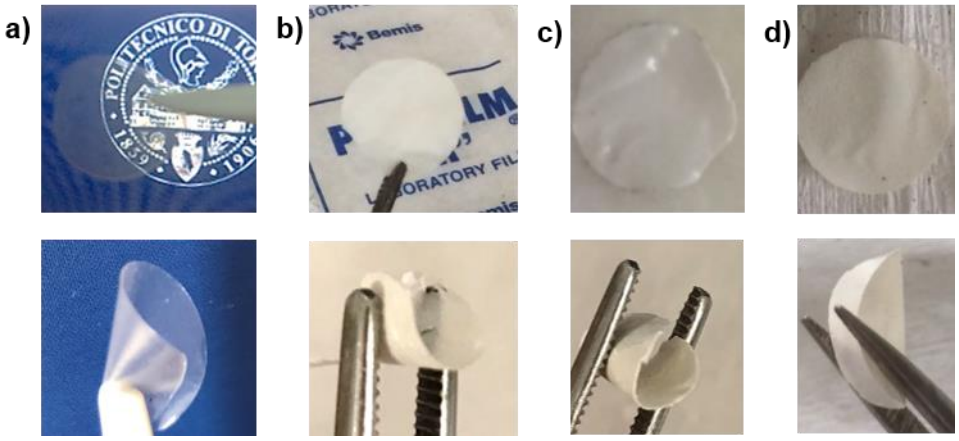

Figure 3

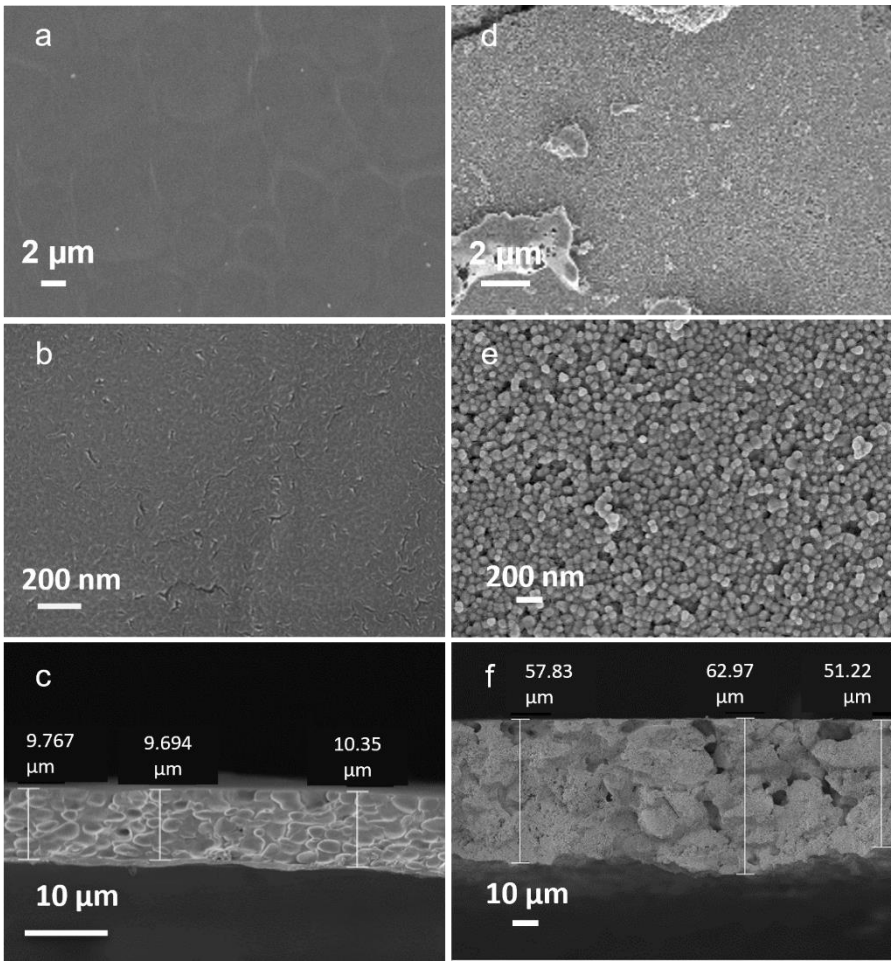
a
2 µm
d
2 µm
b
200 nm
e
200 nm
c
9.767 µm
9.694 µm
10.35 µm
10 µm
f
57.83 µm
62.97 µm
51.22 µm
10 µm

Figure 4

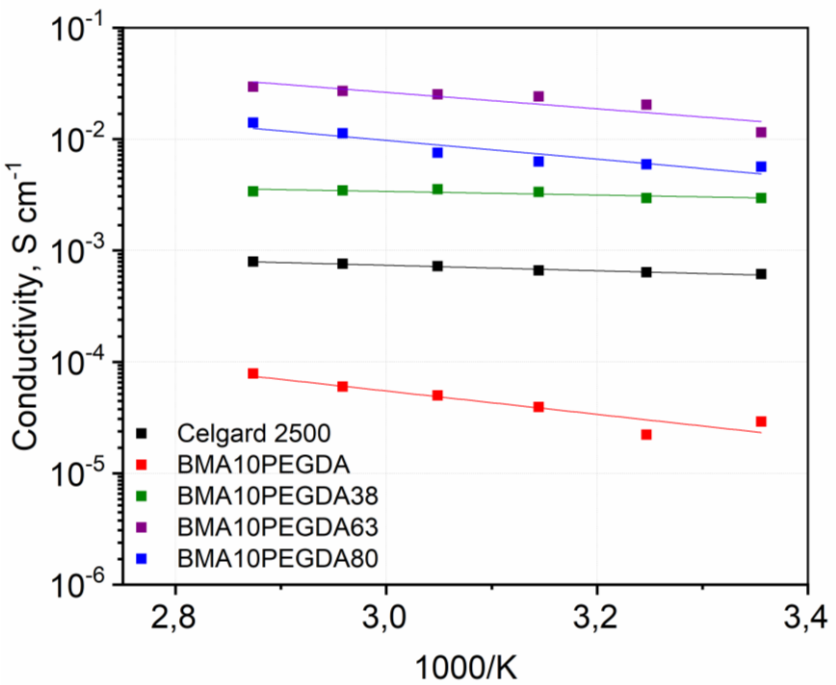

Figure 5

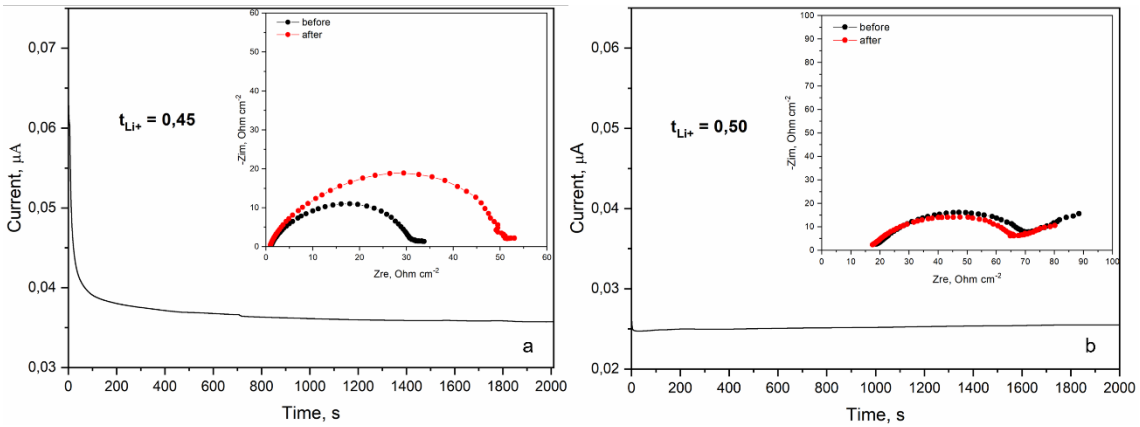

Figure 6

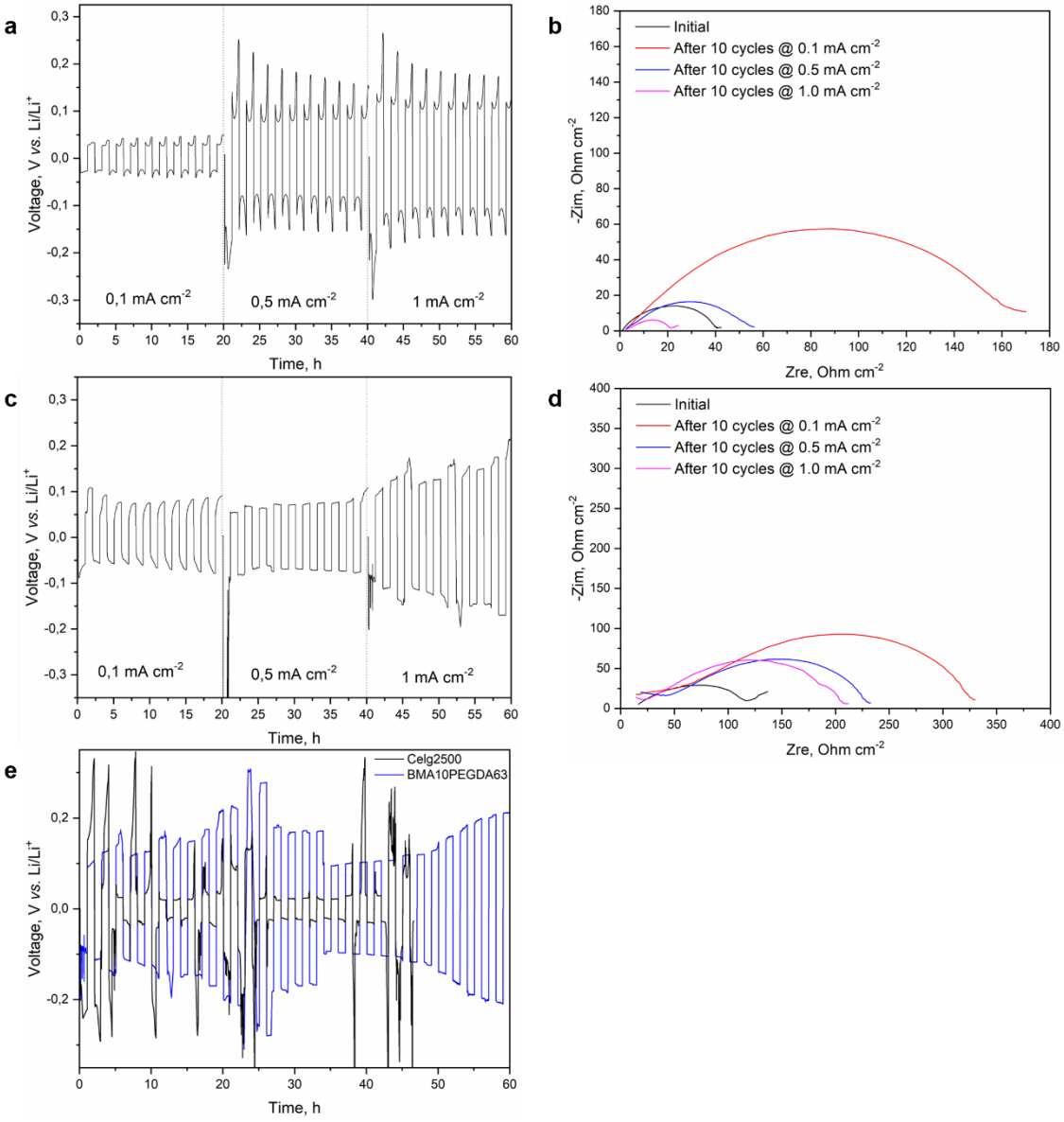
a
Voltage, V vs. Li/Li+
Time, h
0,1 mA cm-2
0,5 mA cm-2
1 mA cm-2
b
Initial
After 10 cycles @ 0.1 mA cm-2
After 10 cycles @ 0.5 mA cm-2
After 10 cycles @ 1.0 mA cm-2
-Zim, Ohm cm-2
Zre, Ohm cm-2
c
Voltage, V vs. Li/Li+
Time, h
0,1 mA cm-2
0,5 mA cm-2
1 mA cm-2
d
Initial
After 10 cycles @ 0.1 mA cm-2
After 10 cycles @ 0.5 mA cm-2
After 10 cycles @ 1.0 mA cm-2
-Zim, Ohm cm-2
Zre, Ohm cm-2
e
Celg2500
BMA10PEGDA63
Voltage, V vs. Li/Li+
Time, h

Figure 7

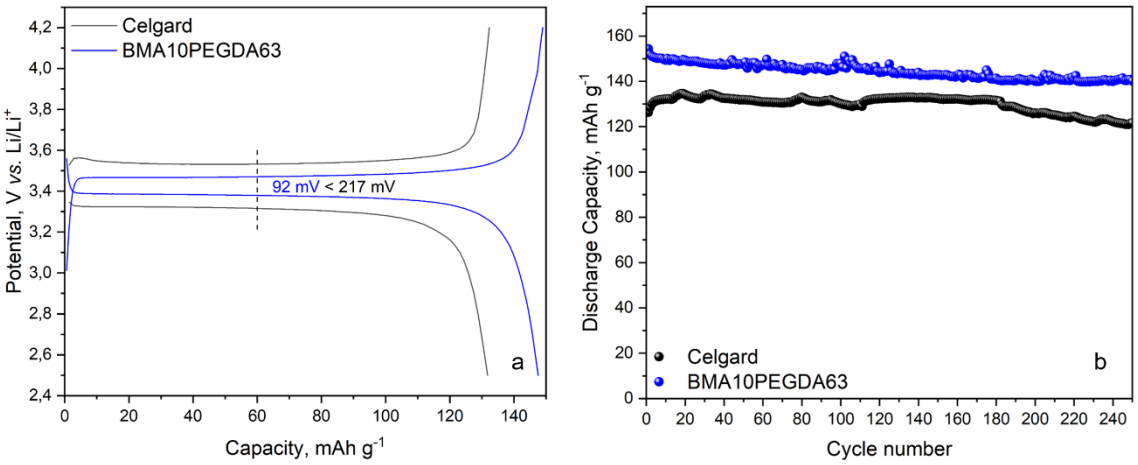
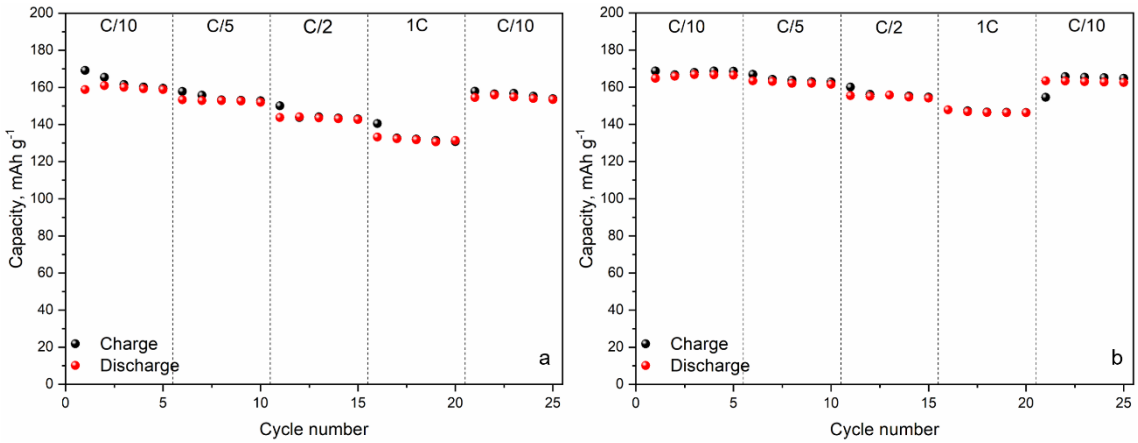
Figure 8